

Article

Tribocorrosion Behavior of γ' -Fe₄N Nitride Layer Formed on Mild Steel by Plasma Nitriding in Chloride-Containing Solution

Yong Sun *  and Richard Bailey

School of Engineering and Sustainable Development, Faculty of Computing, Engineering and Media, De Montfort University, Leicester LE1 9BH, UK; richard.bailey@dmu.ac.uk

* Correspondence: ysun01@dmu.ac.uk

Abstract: Nitriding has long been used to engineer the surfaces of engineering steels to improve their surface and subsurface properties. The role of the surface compound layer (γ' -Fe₄N and/or ϵ -Fe₂₋₃N) in improving the tribological and corrosion-resistant properties of nitrided steels has been established. However, there have been very few studies on the response of the compound layer to tribocorrosion in corrosive environments. In this work, the tribocorrosion behavior of a 5 μ m thick γ' -Fe₄N nitride layer produced on mild steel (MS) by plasma nitriding has been studied in a NaCl-containing solution under various electrochemical conditions. The results show that at a cathodic potential of -700 mV (saturated calomel electrode, SCE), where mechanical wear is predominant, the total material removal (TMR) from the γ' -Fe₄N layer is 37% smaller than that from the untreated MS, and at open circuit potential, TMR from the layer is 34% smaller than that from the untreated MS, while at an anodic potential of -200 (SCE), the γ' -Fe₄N layer can reduce TMR from mild steel by 87%. The beneficial effect of the γ' -Fe₄N nitride layer in improving the tribocorrosion behavior of mild steel is derived from its high hardness and good corrosion resistance in the test solution and its ability to resist both mechanical wear and corrosion and to reduce wear–corrosion synergism.

Keywords: nitriding; iron nitride; wear; corrosion; tribocorrosion; mild steel



Citation: Sun, Y.; Bailey, R. Tribocorrosion Behavior of γ' -Fe₄N Nitride Layer Formed on Mild Steel by Plasma Nitriding in Chloride-Containing Solution. *Lubricants* **2023**, *11*, 281. <https://doi.org/10.3390/lubricants11070281>

Received: 25 May 2023
Revised: 15 June 2023
Accepted: 28 June 2023
Published: 29 June 2023



Copyright: © 2023 by the authors. Licensee MDPI, Basel, Switzerland. This article is an open access article distributed under the terms and conditions of the Creative Commons Attribution (CC BY) license (<https://creativecommons.org/licenses/by/4.0/>).

1. Introduction

Nitriding is a common thermochemical treatment technique used to engineer the surfaces of engineering steels [1–5] and many other metallic materials such as titanium alloys [6,7], aluminum alloys [8,9], nickel-based alloys [10,11] and Co-Cr biomedical alloys [12,13]. In particular, nitriding has long been used in industry to case-harden many steel components such as gears and drive-shafts to improve their performance and durability in real applications [1,2]. This is due to the formation of an iron nitride compound layer on the surface and a nitrogen diffusion zone at the subsurface, which can enhance the wear resistance, fatigue resistance and in many cases, corrosion resistance of steel components [1,14].

During nitriding iron and steels, depending on the nitrogen potential or activity in the treatment media and the steel composition, a compound layer of a few microns thick composed of a single γ' -Fe₄N phase or a mixed γ' -Fe₄N and ϵ -Fe₂₋₃N phase is formed at the surface [2–4]. This is followed by a relatively thick nitrogen diffusion zone at the subsurface. If the steel contains nitride-forming elements such as Cr and V, fine precipitates of nitrides of the alloying elements, such as CrN and VN, will form in the diffusion zone to induce precipitation hardening which contributes to the hardening effect of the diffusion zone [3,15]. In pure iron and plain carbon steels such as mild steels, γ' -Fe₄N needles or thin plates form in the diffusion zone, which provides a marginal hardening effect [15,16]. In such steels, the surface-hardening effect is mainly imparted by the iron nitride compound layer at the surface.

The role of the surface compound layer (γ' -Fe₄N and/or ϵ -Fe_{2,3}N) and the nitrogen diffusion zone in improving the tribological, fatigue and load-bearing capacity properties of nitrided steels has been established [17–20]. The iron nitride compound layer at the surface provides anti-galling properties and good wear resistance, while the nitrogen diffusion zone provides load-bearing capacity and enhances the fatigue strength of steel components, due to the hardening effect and compressive residual stresses [17,19]. In general, a single γ' -Fe₄N phase compound layer of a few microns thick is preferred, because a thick compound layer or a mixed phase compound layer can increase the embrittlement of the surface layer which tends to spall off during service [1–3]. There have also been reports that the iron nitride compound layer can improve the corrosion resistance of steels, such that nitrided steels can be used in more harsh environmental conditions [14,21,22]. Indeed, in many engineering applications, such as in marine and off-shore applications, nitrided components are used in corrosive environments under mechanical contact sliding conditions. Under such conditions, the components are subjected to combined corrosion and mechanical wear actions, i.e., tribocorrosion [23–27]. So far, the studies on the tribocorrosion behavior of nitrided steels have been focused on stainless steels [28,29]. Although there have been a few studies on the tribocorrosion behavior of nitrided low-alloy steels [30,31], the response of the γ' -Fe₄N compound layer to tribocorrosion has not been fully understood. Due to the importance of such a compound layer in determining the performance of nitrided steels, it is necessary to investigate the tribocorrosion behavior of the γ' -Fe₄N layer under various electrochemical conditions.

In the present work, a 5 μm thick γ' -Fe₄N iron nitride layer was produced on mild steel (MS) by plasma nitriding. The tribocorrosion behavior of this γ' -Fe₄N layer was investigated in 1.0% NaCl solution under combined reciprocating sliding wear and electrochemical corrosion conditions. No such systematic study on the response of the technologically important γ' -Fe₄N layer to tribocorrosion has been reported previously. This work provides reference values for researchers and engineers to further explore the application potentials of iron nitride layers to combat material degradation due to tribocorrosion.

2. Materials and Methods

2.1. Substrate Material and Plasma Nitriding

The substrate material was AISI 1020 mild steel with the following chemical composition (in wt%): 0.203 C, 0.463 Mn, ≤ 0.040 P, ≤ 0.050 S, and balance Fe. Low-carbon steel was used to ensure the formation of a pure γ' -Fe₄N layer on the surface by controlled plasma nitriding. The steel was in a normalized state with a ferrite + pearlite structure (Figure 1a) with an average ferrite grain size of 26 μm . The normalizing treatment was conducted in a muffle furnace at 910 $^{\circ}\text{C}$ for 20 min, followed by air cooling. Specimens of 25 \times 15 \times 4 mm dimensions were machined from a steel plate. The surface to be nitrided (25 \times 15 mm) was manually ground using SiC grinding papers down to the P1200 grade to achieve a surface finish of 0.2 μm (R_a).

Plasma nitriding was carried out at 550 $^{\circ}\text{C}$ in a plasma atmosphere containing 10% N₂ and 90% H₂, at a treatment pressure of 3 mbar for 5 h. Before nitriding, the surface was cleaned in running water and then in ethanol ultrasonically for 10 min. After plasma nitriding, the specimens were cooled inside the furnace under vacuum (0.1 mbar) down to room temperature.

Figure 1 shows the cross-sectional morphology of the nitrided specimen. Table 1 summarizes the structural features of the nitrided (PN) and un-nitrided (normalized) specimens. It can be seen that plasma nitriding produced a thin “white layer” about 5 μm thick at the surface (Figure 1b) and a relatively thick diffusion zone about 300 μm thick beneath (Figure 1a). X-ray diffraction analysis confirmed that the “white layer” at the surface was composed of γ' -Fe₄N phase, as can be seen from Figure 2, which shows that only γ' and α -Fe were detected, where the α -Fe peaks came from the substrate. In the nitrogen diffusion zone, γ' -Fe₄N needles were formed, which is typical of nitriding pure iron and low-carbon steels [15,16]. The surface hardness of the PN and normalized

specimens were also measured under various indentation loads and the results are listed in Table 1. Clearly, the nitrided surface exhibited a higher hardness than the un-nitrided surface. At the small indentation load of 25 g, the surface hardness of the PN specimen was 760 HV, which agrees with the reported hardness value of γ' -Fe₄N [32]. With increasing indentation load, the surface hardness of the PN specimen declined quickly, due to the increasing substrate effect. This also suggests that the precipitation of γ' -Fe₄N needles in the diffusion zone had a limited hardening effect. Microhardness measurements were also made in the diffusion zone below the γ' -Fe₄N layer. The hardness of the diffusion zone ranged from 245 to 255 HV_{0.1}, similar to that measured from the normalized substrate. Thus, the surface-hardening effect was mainly derived from the formation of the γ' -Fe₄N layer.

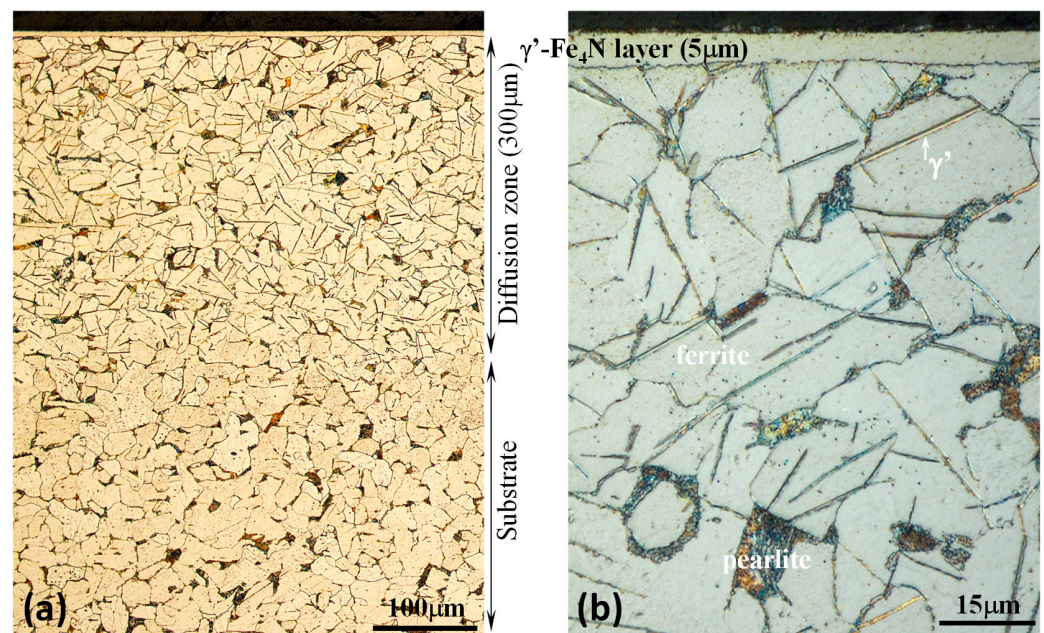


Figure 1. Microscopic images of the nitrided mild steel specimen showing (a) the overall view of the cross section from the surface to the substrate and (b) details of the 5 μm thick Fe₄N compound layer at the surface and the underneath diffusion zone with needle-like precipitates.

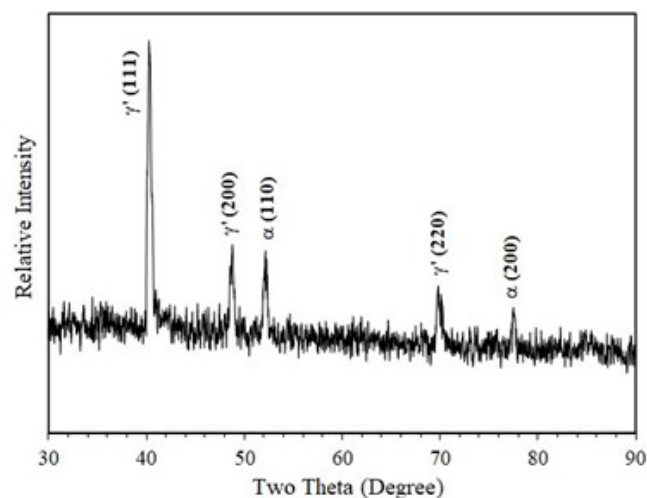


Figure 2. X-ray diffraction pattern generated from the nitrided specimen, showing that the compound layer was composed of γ' -Fe₄N phase (Cu K_α radiation).

Table 1. Summary of structure and surface hardness of the test specimens.

Specimen	Structure		Surface Hardness			
	Surface Layer	Diffusion Zone	HV _{0.025}	HV _{0.05}	HV _{0.1}	HV _{0.2}
PN MS	γ' -Fe ₄ N 5 μ m thick	γ' -Fe ₄ N needles in α + P matrix	760 \pm 17	540 \pm 14	370 \pm 9	292 \pm 7
Raw MS	α + P	α + P	266 \pm 15	258 \pm 13	248 \pm 9	245 \pm 7

Note: α —ferrite; P—pearlite.

2.2. Corrosion Tests

All corrosion tests were conducted at room temperature in 1.0 wt% NaCl solution by dissolving analytical grade NaCl in double-distilled water. This solution was used because it contains a chloride content similar to that in human body fluids. An ACM Gill AC potentiostat (ACM Gill AC, ACM Ltd., Cumbria, UK) was used to measure the potentials and currents during the tests employing a 3-electrode configuration, i.e., the test specimen as the working electrode, a saturated calomel electrode (SCE) as the reference electrode and a platinum mesh as the auxiliary electrode.

Before corrosion tests, the nitrided and un-nitrided surfaces were slightly polished using 1 μ m diamond paste to remove surface contaminants resulting from nitridding and to further smoothen the surface. This was followed by ultrasonic cleaning in ethanol for 10 min. Then the specimen was masked by using an insulating lacquer to leave a test window of 10 mm \times 10 mm which would be exposed to the solution.

Corrosion tests were conducted both potentiodynamically to measure the anodic polarization curves of the specimens and potentiostatically to measure the current evolution as a function of time at constant potentials. The potentiodynamic test was conducted at a scan rate of 1 mV/s, by sweeping potential from -200 mV (vs. open circuit potential (OCP)) to 800 mV (vs. OCP). The potentiostatic tests were conducted at a cathodic potential of -700 mV(SCE), at OCP and at an anodic potential of -200 mV(SCE). During all the tests, the current and potential values were recorded continuously at a sampling rate of 1 Hz.

2.3. Tribocorrosion Tests

Tribocorrosion tests were carried out under the same electrochemical conditions and following the same surface preparation procedures as those used in the corrosion tests described in Section 2.2. A laboratory-scale reciprocating wear test machine was used to perform the tests [33]. The tribometer allowed for the reciprocating movement of a flat specimen against a stationary slider (ball) at controlled frequency, stroke amplitude and contact load, and the continuous measurement of friction force by the incorporated load cell. The incorporation of an electrochemical potentiostat with the tribometer allowed for the measurements of potential and current during the sliding wear process. Before the test, the specimen was masked by using an insulating lacquer to leave a test window of 15 mm \times 3 mm which would be exposed to the solution. An electrically conducting lead was connected to the specimen to ensure conductivity of the specimen for electrochemical measurements. In order to ensure that electrochemical reactions only occur in the test window, all other fixtures, including the specimen holder, the test cell and the slider holder were made of nylon.

During tribocorrosion testing, the specimen was immersed in the 1.0 wt% NaCl solution. An SCE and a platinum wire were also inserted in the solution as the reference and auxiliary electrode, respectively. An alumina (Al₂O₃) ball of 8 mm diameter ($R_a = 0.05$ μ m) was used as the stationary slider, which made sliding contact with the reciprocating specimen, generating a sliding track on the specimen. All tests were implemented under a contact load of 4 N for a total sliding duration of 7200 s at a reciprocating frequency of 1 Hz and an amplitude of 6 mm. Before and after sliding, the specimen was stabilized in the solution for 300 s under respective conditions, such that potentials and/or currents could

be measured before, during and after sliding. The test parameters were selected based on our experience and preliminary tests to ensure that the properties of the γ' -Fe₄N layer were measured.

All corrosion and tribocorrosion tests were duplicated, which was considered sufficient because the results were reproducible. The results from the two tests are presented where applicable. Table 2 summarizes the test conditions under both sliding (tribocorrosion) and no-sliding (corrosion) conditions.

Table 2. Summary of corrosion and tribocorrosion conditions.

	Corrosion	Tribocorrosion
Potentiodynamic	–200 mV to 800 mV, 1 mV/s No sliding	–200 mV to 800 mV, 1 mV/s Sliding at 4 N and 1 Hz
Potentiostatic	–700 mV(SCE) no sliding OCP no sliding –200 mV(SCE) no sliding	–700 mV(SCE) sliding at 4 N and 1 Hz OCP sliding at 4 N and 1 Hz –200 mV(SCE) sliding at 4 N and 1 Hz

2.4. Specimen Characterization

After corrosion and tribocorrosion tests, the corroded surfaces and sliding tracks were examined microscopically under optical microscope (Nikon LV150N, Nikon, Tokyo, Japan) and scanning electron microscope (SEM) (Carl Zeiss EVO LS 15, Carl Zeiss, Jena, Germany). Using the extended depth-of-focus feature of the Nikon microscope, 3D images and surface profiles of the sliding tracks could be captured. The SEM was equipped with EDX facilities for elemental composition analysis. A profilometer (Surtronic Intra Touch, Taylor-Hobson, Leicester, UK) was used to measure the surface profiles across each sliding track at three locations to measure the cross-sectional area of the track and thus obtain the total material removal (TMR) from each specimen due to tribocorrosion.

3. Results

3.1. Potentiodynamic Tests

Figure 3a shows the anodic polarization curves measured without sliding and during sliding for the un-nitrided (normalized) and plasma-nitrided (PN) specimens. Under the condition of corrosion (no-sliding), the normalized specimen showed active anodic dissolution behavior: the current density increased quickly at anodic potentials above the corrosion potential and then increased slowly due to transpassivity. Microscopic examination revealed that the normalized specimen suffered from severe corrosion which etched the grain structures and led to grain detachment (see Figure 4a). Under the same no-sliding condition, the PN specimen showed a higher corrosion potential and much lower current densities in the anodic region. The corroded area only showed some discoloration as compared to the un-corroded area (see Figure 4b). Thus, in the test solution, the normalized specimen was in the active state in the anodic region, while the γ' -Fe₄N layer formed on the surface by nitriding was effective in reducing the dissolution rate of mild steel. Under the condition of tribocorrosion (sliding), the corrosion potentials of both specimens were shifted cathodically and the current densities in the anodic region were increased (Figure 3a). This demonstrates that the sliding mechanical action activated both the normalized surface and PN surface such that corrosion in the sliding tracks was accelerated, which is a common phenomenon observed in tribocorrosion [23–27].

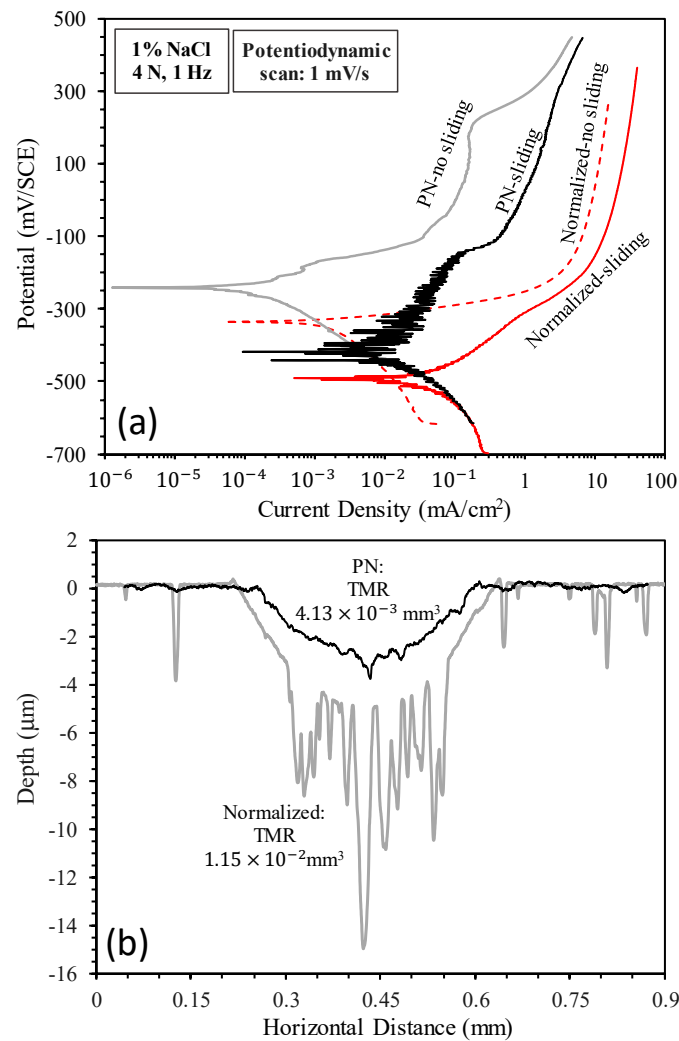


Figure 3. (a) Anodic polarization curves measured without sliding and during sliding and (b) surface profiles measured across the sliding tracks produced during anodic polarization.

Table 3 lists the corrosion potentials, corrosion current densities and corrosion rates derived from the polarization curves shown in Figure 3a. It can be seen that sliding led to an increase in corrosion current density by an order of magnitude for the normalized specimen and by nearly two orders of magnitude for the PN specimen. As compared to the normalized specimen, the PN specimen showed higher corrosion potentials and lower corrosion current densities, demonstrating that the γ' -Fe₄N layer had the ability to reduce corrosion under both sliding and no-sliding conditions.

Table 3. Corrosion potential (E_{corr}), corrosion current density (i_{corr}) and corrosion rate derived from the polarization curves in Figure 3a.

Specimen	E_{corr} (mV/SCE)		i_{corr} (mA/cm ²)	
	No Sliding	Sliding	No Sliding	Sliding
Raw MS	-335	-490	4.28×10^{-3}	4.95×10^{-2}
PN MS	-241	-418	2.05×10^{-4}	1.91×10^{-2}

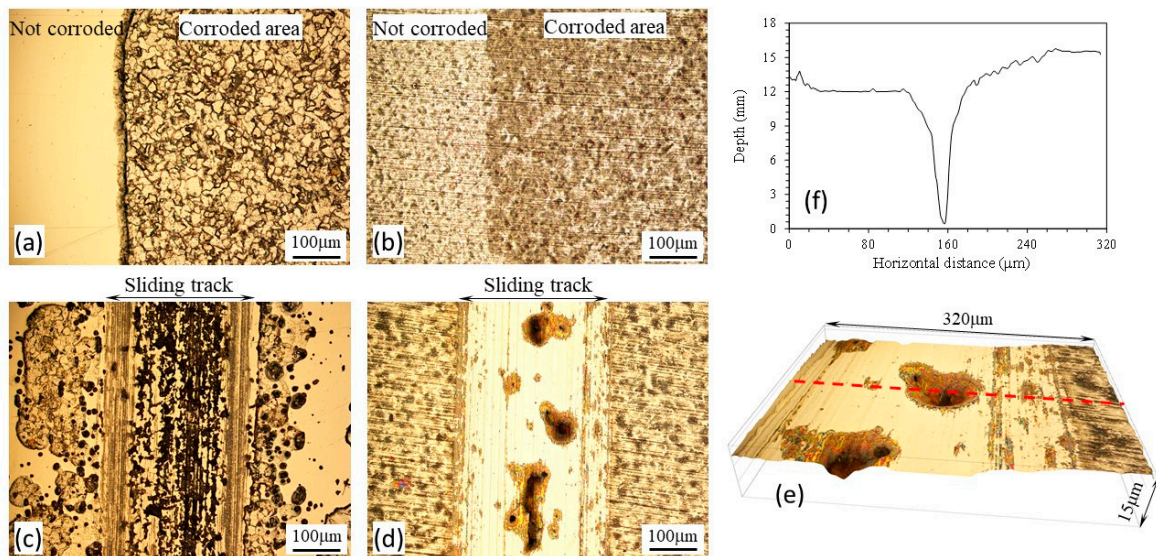


Figure 4. Microscopic images showing the test surfaces after potentiodynamic polarization tests without sliding and during sliding: (a) Normalized MS without sliding; (b) PN MS without sliding; (c) Normalized MS with sliding; (d) PN MS with sliding; (e) 3D view of corrosion pits in (d); (f) surface profile measured across a pit shown by the dashed line in (e).

Figure 3b shows the surface profiles measured across the sliding tracks after anodic polarization tests during sliding. It can be seen that the sliding track on the normalized specimen was much deeper and rougher than that on the PN specimen. Material removal from outside the sliding track of the normalized specimen was also evident, obviously due to corrosion occurring outside the sliding track, as can be seen from Figure 4c. The deep valleys in the sliding track shown in Figure 3b for the normalized specimen were the results of accelerated corrosion. On the other hand, the sliding track on the PN specimen exhibited a shiny and polished appearance (Figure 4d). The TMR from the PN specimen was 64% smaller than that from the normalized specimen (Figure 3b). The measured surface profile shown in Figure 3b also revealed that the sliding track on the PN specimen was smaller than $4 \mu\text{m}$, thus tribocorrosion occurred mainly within the $\gamma'- Fe_4N layer. However, some pits of several tens of microns in size were observed in the sliding track (Figure 4d,e). The penetration depth of the pits was as deep as $15 \mu\text{m}$ (Figure 4f), suggesting that once the $\gamma'- Fe_4N layer was broken down locally, accelerated corrosion happened in the form of pitting corrosion during the tribocorrosion process.$$

The results presented in this section provide a general picture of the corrosion and tribocorrosion behavior of the specimens over a wide potential range. In order to further demonstrate the beneficial effect of the $\gamma'- Fe_4N layer in improving the tribocorrosion behavior of mild steel, detailed tests were conducted potentiostatically at different potentials, as discussed in the following sections.$

3.2. Cathodic Potential Tests

Figure 5a shows the recorded current versus time curves at the cathodic potential of -700 mV(SCE) in 1.0% NaCl solution under both sliding and no-sliding conditions. Under no-sliding conditions, negative currents were recorded for both specimens, suggesting that cathodic reactions were dominant, while metal oxidation (corrosion) became less dominant [23]. Sliding led to an increase in cathodic currents from around -0.04 mA to around -0.1 mA for both specimens, suggesting that the sliding action activated the surfaces and accelerated cathodic reactions.

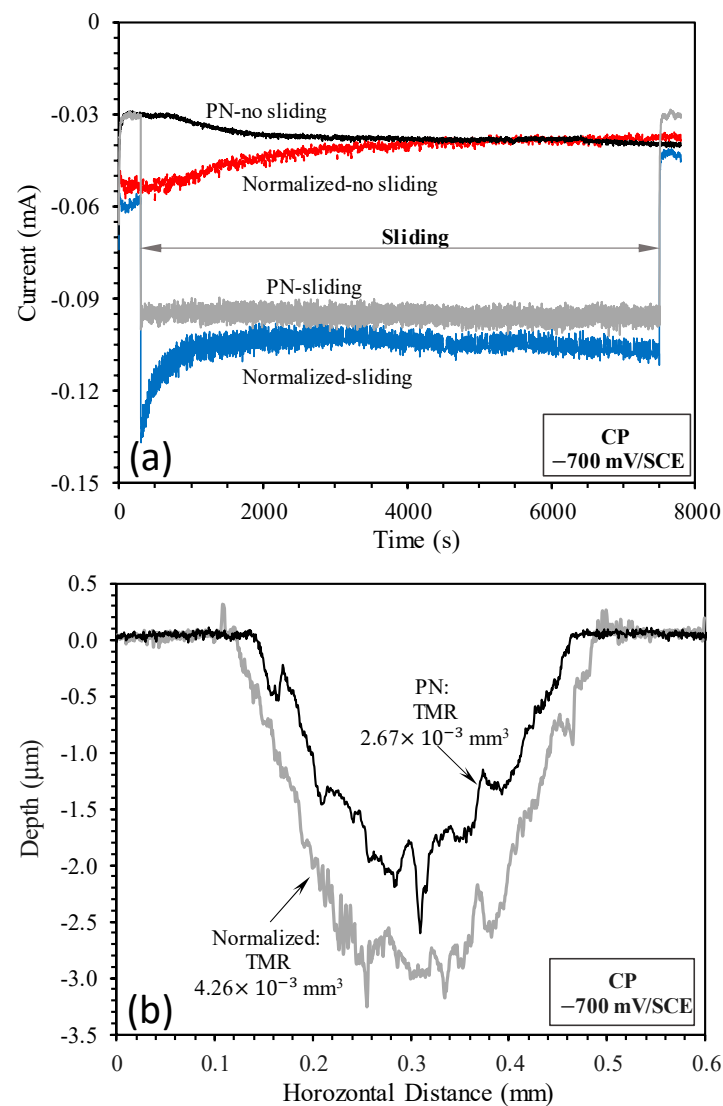


Figure 5. (a) Current variation with time measured without sliding and during sliding at the cathodic potential of -700 mV(SCE) and (b) surface profiles measured across the sliding tracks produced by sliding at -700 mV(SCE) .

Although corrosion is still possible at such a cathodic potential, its contribution to TMR from the sliding track is insignificant [23,33]. Thus, TMR was mainly due to mechanical wear. Figure 5b shows the surface profiles measured across the sliding tracks on the normalized and PN specimens. It can be seen that the sliding track on the normalized specimen was deeper and wider than that on the PN specimen. The wear depth on the PN specimen was smaller than $3 \mu\text{m}$, thus wear occurred within the $5 \mu\text{m}$ thick $\gamma\text{-Fe}_4\text{N}$ layer. The TMR from the PN specimen was about 63% of that from the normalized specimen. Clearly, the $\gamma\text{-Fe}_4\text{N}$ layer had the ability to reduce the mechanical wear of mild steel by about 37%.

Figure 6 shows the SEM images and EDX elemental mappings of the sliding tracks on the normalized and PN specimens. The parallel scratch marks on the sliding tracks are good indications of mechanical abrasion wear arising from the sliding action of the alumina slider. The sliding track on the PN specimen showed a shiny appearance with very few signs of corrosion (Figure 6b). EDX mapping could not find oxygen on the worn surface, instead, nitrogen was found (Figure 6b), further confirming that the $\gamma\text{-Fe}_4\text{N}$ layer was not worn through. On the other hand, the sliding track on the normalized specimen was covered

with some dark gray products, which were rich in oxygen (Figure 6a), suggesting that limited corrosion could happen to the normalized specimen at such a cathodic potential.

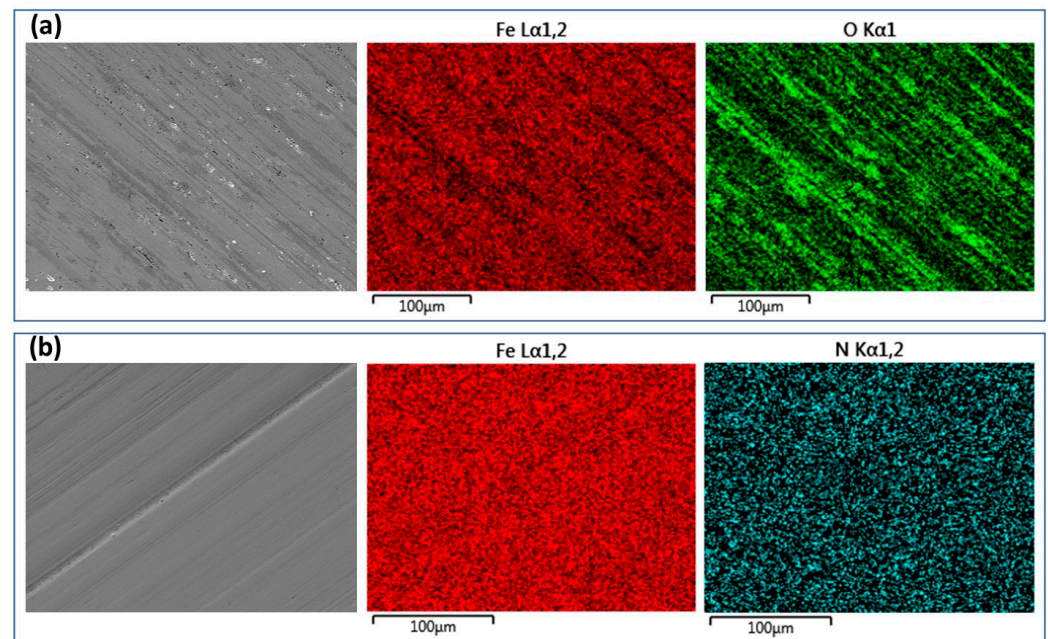


Figure 6. Microscopic images and EDX mapping of the sliding tracks produced at the cathodic potential of -700 mV(SCE) on the (a) normalized MS and (b) PN MS specimens.

3.3. Open Circuit Potential (OCP) Tests

The OCP versus time curves recorded under open circuit conditions are shown in Figure 7a. Under no-sliding conditions, the OCP of both specimens decreased with increasing time of immersion in the solution. Both specimens were in the active state such that the surfaces became more activated with increasing time of immersion, leading to decreased OCP values. Under sliding conditions, the recorded OCP values also decreased with time and were more negative than those measured under no-sliding conditions, suggesting that sliding led to further activation of the surfaces. In agreement with the potentiodynamic measurements shown in Figure 3a, the OCP values measured for the PN specimen were more anodic than those measured for the normalized specimen under both sliding and no-sliding conditions. Clearly, the normalized surface was in a more active state than the PN surface under open circuit conditions.

The surface profiles measured across the sliding tracks are shown in Figure 7b. The sliding track on the normalized specimen was deeper than that on the PN specimen. Interestingly, material removal also occurred outside the sliding track on the normalized specimen, which was due to corrosion in areas exposed to the solution outside the track, as can be seen from Figure 8a. On the other hand, corrosion outside the sliding track on the PN specimen was very limited (Figure 7b), which was confirmed by microscopic examination (Figure 8c). Inside the sliding track, there were clear signs of corrosion in addition to the parallel abrasion marks (Figure 8b,d). The wear depth of the PN specimen was smaller than $5\ \mu\text{m}$ (Figure 7b), thus wear and corrosion occurred within the γ' - Fe_4N layer. A few pits were also observed inside the sliding track on the normalized specimen, which were several microns in depth (Figure 8b).

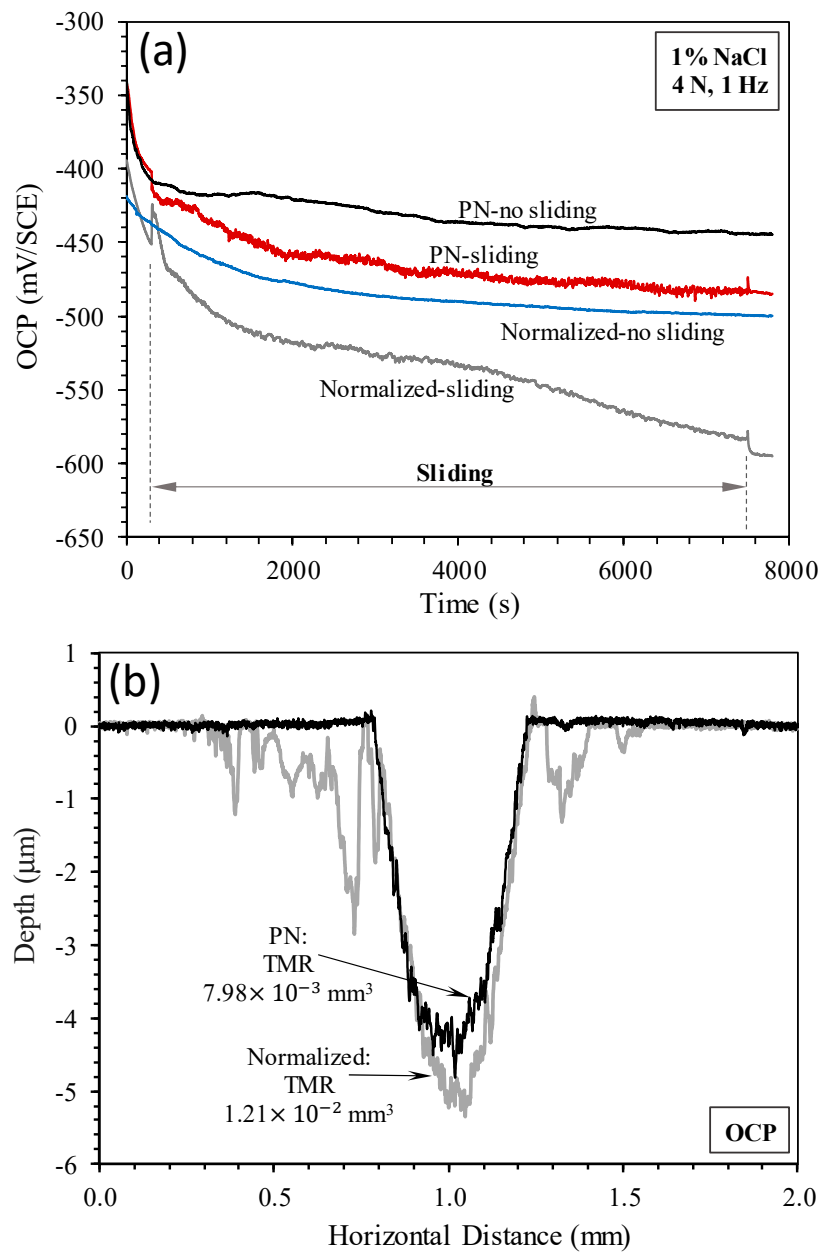


Figure 7. (a) Open circuit potential (OCP) variation with time measured without sliding and during sliding at OCP and (b) surface profiles measured across the sliding tracks produced by sliding at OCP.

TMRs from the specimens were obviously the combined results of wear (abrasion) and corrosion. TMR from the PN specimen was about 34% smaller than that from the normalized specimen (Figure 7b). When compared with TMRs resulting from sliding at the cathodic potential of -700 mV(SCE) discussed in Section 3.2, TMR at OCP was 2.8 times larger for the normalized specimen and 3.6 larger for the PN specimen. This demonstrates the effect of corrosion and wear–corrosion synergism in accelerating TMR from the specimen.

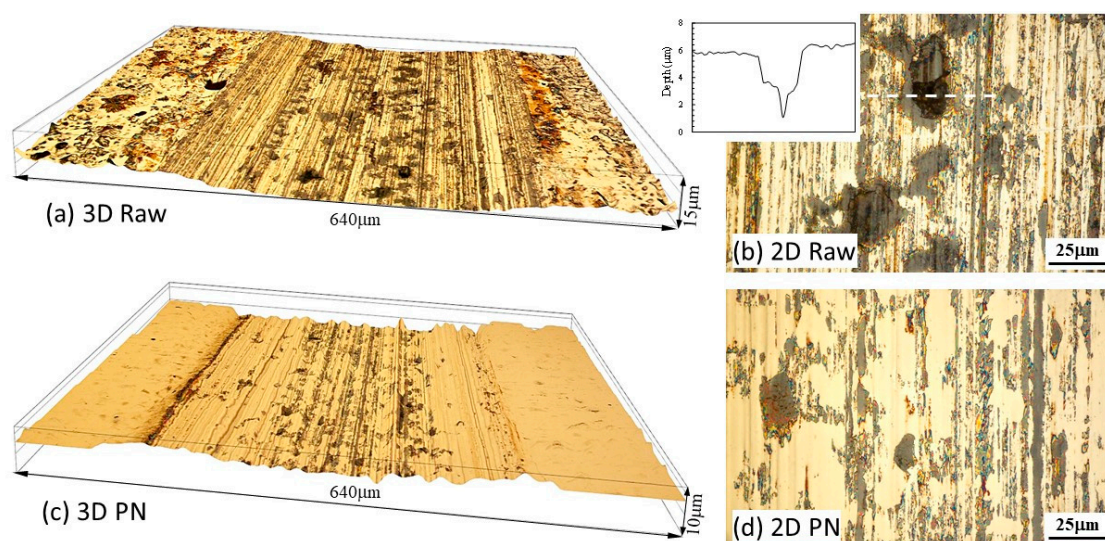


Figure 8. Microscopic images showing 3D (a,c) and 2D (b,d) views of the sliding tracks produced at OCP on the normalized MS (a,b) and PN MS (c,d) specimens. The inset in (b) shows the surface profile measured across the pit indicated by the dashed line.

3.4. Anodic Potential Tests

At the anodic potential of -200 mV(SCE), the normalized and PN specimens behaved quite differently (Figure 9a). Under no-sliding conditions, both the normalized and PN specimens registered continuously increasing the currents with polarization time, confirming that the specimens suffered from anodic dissolution and had no ability to passivate at such an anodic potential. However, the current generated from the PN specimen was more than two orders of magnitude smaller than that generated from the normalized specimen (Figure 9a,b), demonstrating that the γ' -Fe₄N layer had the ability to reduce metal dissolution and improve corrosion resistance.

Interestingly, sliding led to a decrease in currents from the normalized specimen (Figure 9a), which is different from the observations made on passive metals where sliding leads to an abrupt increase in currents due to the depassivation of the surface by the sliding action [24,25,33]. For the active normalized specimen in this study, removal of the corrosion products from the sliding track by the mechanical action obviously helped to reduce metal dissolution. After the termination of sliding, the current from the normalized specimen increased to the level measured under no-sliding conditions. A microscopic examination revealed that corrosion occurred both inside and outside the sliding track of the normalized specimen (Figure 10). Outside the sliding track, the surface became quite rough with peaks and valleys due to grain detachment arising from the corrosion action (Figure 10b). Inside the sliding track, the peaks were flattened due to the wearing action, but the valleys and some corrosion pits could still be observed (Figure 10a).

On the other hand, sliding led to an abrupt increase in currents from the PN specimen, and the current generated during sliding increased slowly for the first 2000 s, and then increased more quickly between 2000 s and 4000 s sliding, and then further quickly after 4000 s sliding (Figure 9b). Microscopic examination (Figure 11) revealed that in the central region of the sliding track on the PN specimen, the γ' -Fe₄N layer was removed, such that pits were formed in this region, which penetrated deep into the substrate (Figures 9c and 11). This explains the quick increase in currents after 2000 s and then 4000 s sliding (Figure 9b).

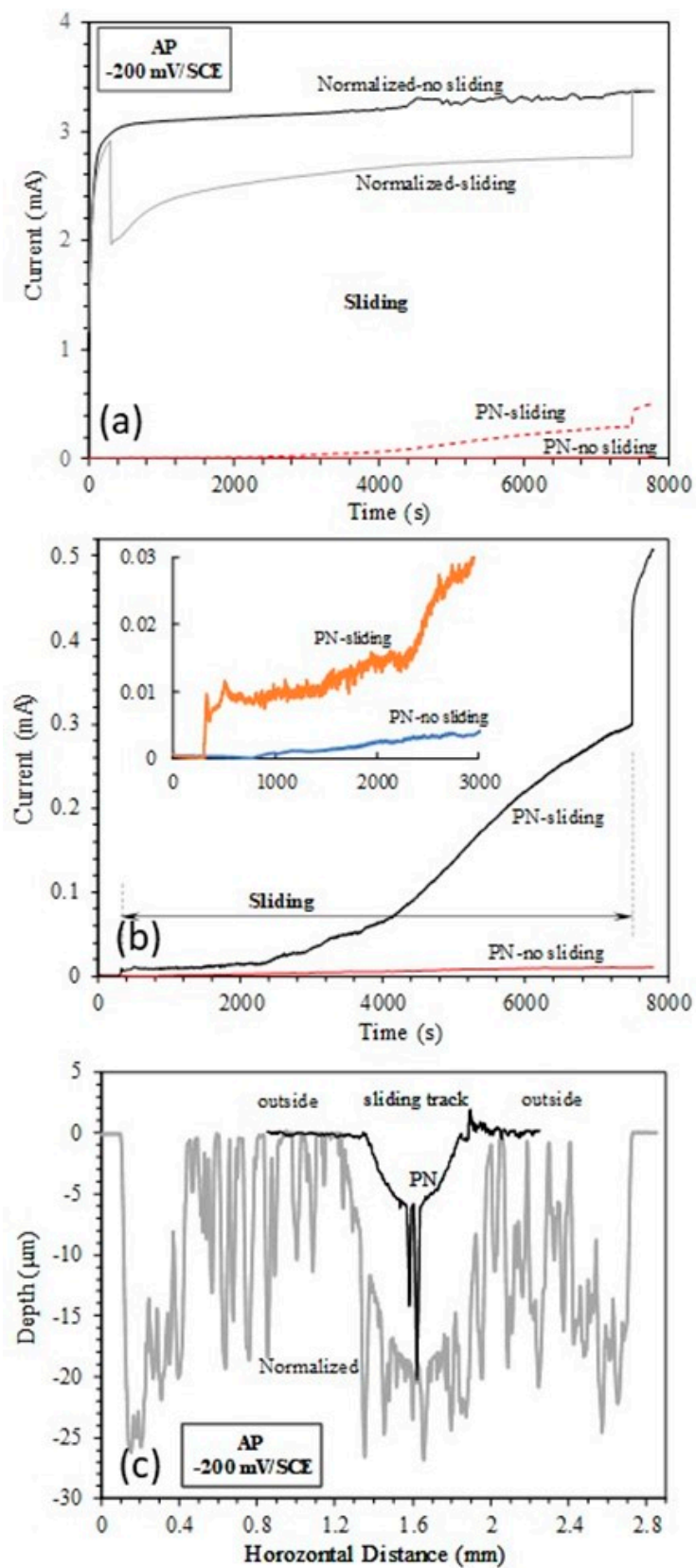


Figure 9. (a) Current variation with time measured without sliding and during sliding at the anodic potential of -200 mV(SCE) ; (b) Zoom-in view of current variation of the nitrated specimen during sliding at -200 mV(SCE) ; (c) Surface profiles measured across the sliding tracks produced by sliding at -200 mV(SCE) .

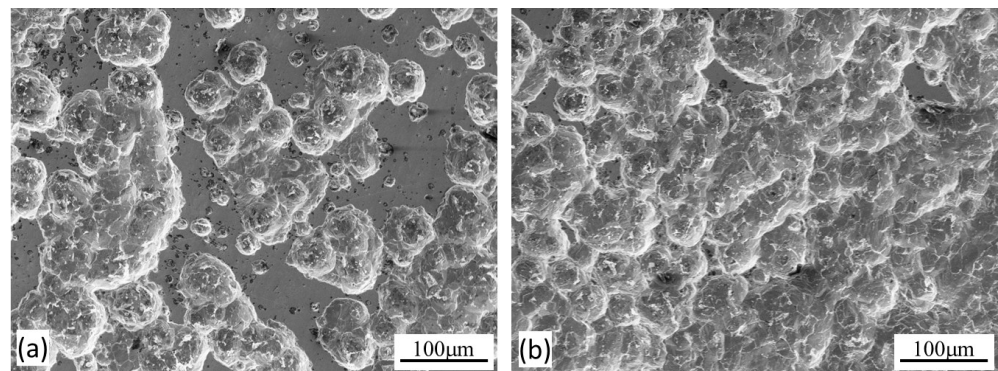


Figure 10. Microscopic images showing (a) the worn surface inside the sliding track and (b) the corroded surface outside the sliding track, produced at the anodic potential of -200 mV(SCE) on the normalized MS.

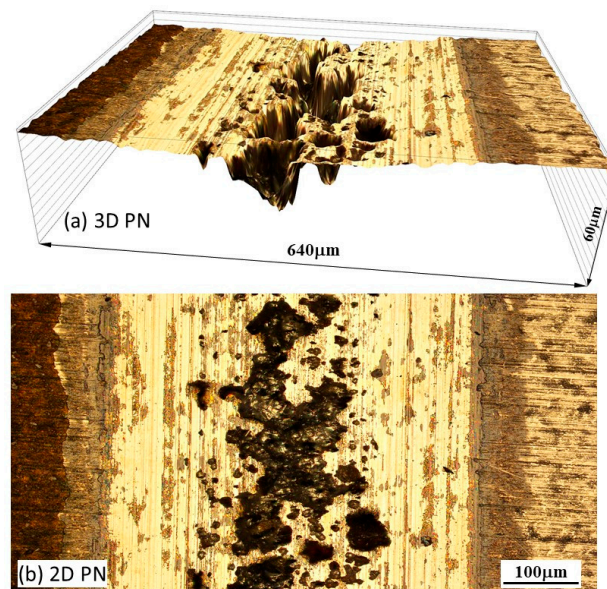


Figure 11. Microscopic images showing (a) 3D and (b) 2D views of the sliding track, produced at the anodic potential of -200 mV(SCE) on the PN MS.

Surface profile measurements across the sliding tracks showed that TMR from the PN specimen was mainly from the sliding track with limited corrosion loss outside the sliding track (Figure 9c). The wear depth in the central region of the sliding track was more than 5 μm and as deep as 20 μm in the pitting area, suggesting that the γ' - Fe_4N layer was worn through in this region, in line with the microscopic examination (Figure 11). On the other hand, for the normalized specimen, TMR came from both inside and outside the sliding track (Figure 9c). Thus, corrosion played a more significant role in TMR from the normalized specimen.

4. Discussion

4.1. Effect of Potential on Tribocorrosion Behavior

From the results presented in Section 3, the 5 μm γ' - Fe_4N thick layer was not worn through during the tribocorrosion tests. Thus, the measured corrosion and tribocorrosion behavior of the nitride specimen is characteristic of the γ' - Fe_4N layer. It is clear that the γ' - Fe_4N layer produced by nitriding on mild steel has the ability to increase surface hardness, reduce metal dissolution rate and improve tribocorrosion resistance in the NaCl-containing solution. The tribocorrosion behavior of the γ' - Fe_4N layer is affected by the

applied potential, as summarized in Figure 12, which shows the variation of the average coefficient of friction (COF) and TMR with potential.

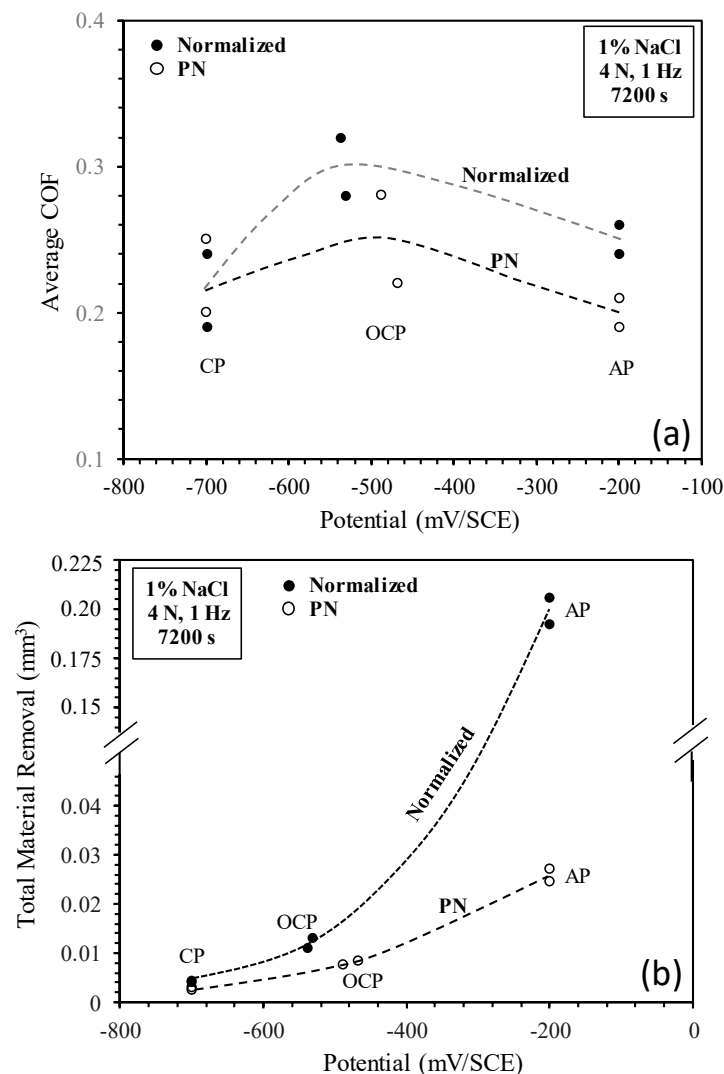


Figure 12. (a) Average coefficient of friction (COF) and (b) total material removal during sliding at cathodic (CP), open circuit (OCP) and anodic (AP) potentials.

The COF values vary quite largely between two repeated tests under the same conditions (Figure 12a). However, a general trend can be seen that the average COF for both specimens is the highest at OCP and is lower at cathodic and anodic potentials. This behavior can be explained as follows. At the cathodic potential of -700 mV(SCE), mechanical wear is predominant and there is little contribution of corrosion products to friction. At OCP, both mechanical wear and corrosion are involved and there is synergism between wear and corrosion, which could lead to increased friction because of the trapping of corrosion-wear products at the frictional interface. At the anodic potential of -200 mV(SCE), although corrosion is accelerated, the formation of corrosion pits, particularly at the central region of the sliding track on the PN specimen (Figure 11), could reduce the real contact area and thus could lead to reduced friction. As compared to the normalized specimen, the PN specimen shows lower friction at OCP and -200 mV(SCE), thus the γ' -Fe₄N layer is beneficial in reducing friction during tribocorrosion in the NaCl-containing solution.

The variation of TMR with potential is shown in Figure 12b. It can be seen that the TMR of both specimens increases with potential and the TMR of the PN specimen is significantly lower than that of the normalized specimen under all test conditions. As the

potential is increased from OCP to -200 mV(SCE), the TMR of the normalized specimen is increased by nearly 17 times, while the TMR of the PN specimen is increased only by 3 times. When comparing the TMR of the two specimens, the TMR of the PN specimen is 37% lower at the cathodic potential, 34% lower at OCP and 87% lower at the anodic potential than the normalized specimen. This demonstrates the beneficial effect of the γ' -Fe₄N layer on improving the resistance to mechanical wear, corrosion and the synergism between wear and corrosion of mild steel, as discussed below.

4.2. Contribution of Mechanical Wear, Corrosion and Wear–Corrosion Synergism

Material removal during tribocorrosion is the result of mechanical wear, corrosion and synergism between wear and corrosion [26,27,34,35]. At the cathodic potential, corrosion is limited and mechanical wear is dominant. The results (Figures 5b and 12b) show that the TMR of the PN specimen is 37% smaller than that of the raw specimen. This can be attributed to the high hardness of the γ' -Fe₄N layer (Table 1), which provides good resistance to mechanical abrasive wear. At OCP and the anodic potential, both mechanical wear and corrosion are involved and there is synergism between wear and corrosion. According to the synergistic approach for tribocorrosion analysis [23,26], the TMR (T) is the sum of material removal due to mechanical wear (W_0), corrosion (C_0) and the synergism between wear and corrosion (S):

$$T = W_0 + C_0 + S \quad (1)$$

where T can be measured after the tests (e.g., Figure 12b), W_0 is the TMR during sliding at the cathodic potential (-700 mV (SCE)) and C_0 can be theoretically estimated by using the Faraday's law [23,26,27]:

$$V_{chem} = \frac{ItM}{nF\rho} \quad (2)$$

where I is corrosion current (A) measured under no-sliding conditions, t (s) is the sliding time, M (g/mol) is the atomic mass of the steel, n is the valence of oxidation, which is 3 to account for FeOOH oxide film on steel, which is the main corrosion product of carbon steel [36,37], F is the Faraday's constant (96,458 C/mol) and ρ is the density of steel.

Equation (2) can be used to calculate C_0 if general corrosion is the predominant form of corrosion. In the present work, at the anodic potential of -200 mV(SCE), significant pitting corrosion occurred inside the sliding track (Figures 10 and 11), particularly in the central region of the sliding track on the PN specimen, thus most of the measured currents (Figure 9a,b) are expected to come from the corrosion pits. In such a case, it is unrealistic to estimate C_0 by using Equation (2). However, at OCP, general corrosion was predominant, thus the corrosion parameter data (i_{corr} under no-sliding conditions) shown in Table 3 can be used to estimate C_0 for both specimens and then Equation (1) can be used to calculate S . The results are summarized in Table 4.

Table 4. Summary of T , W_0 , C_0 , ΔC and ΔW at OCP.

Specimen	T (mm ³)	W_0 (mm ³)	C_0 (mm ³)	S (mm ³)	$S/T \times 100$	DC (mm ³)	DW (mm ³)
Normalized	1.21×10^{-2}	4.26×10^{-3}	5.03×10^{-4}	7.28×10^{-3}	60.1	5.31×10^{-3}	1.97×10^{-3}
PN	7.98×10^{-3}	2.67×10^{-3}	2.39×10^{-5}	5.29×10^{-3}	66.3	2.20×10^{-3}	3.09×10^{-3}

From Table 4, it can be seen that at OCP, as compared to the normalized specimen, the γ' -Fe₄N layer can reduce mechanical wear by 37%, corrosion by 95% and wear–corrosion synergism by 27%. The contribution of corrosion to TMR is smaller than 5% for the normalized specimen and smaller than 1% for the γ' -Fe₄N layer. On the other hand, the synergistic effect has a large contribution to TMR for both specimens, accounting for 60.1% of TMR for the normalized specimen and 66.3% of TMR for the PN specimen (refer to the $S/T \times 100$ column in Table 4). Therefore, it can be concluded that the γ' -Fe₄N layer has the

ability to provide improved resistance to mechanical wear, corrosion and wear–corrosion synergism. It is also noted that the contribution of the synergistic effect of the γ' -Fe₄N layer to TMR (66.3%) is larger than that of the normalized specimen (60.1%); to explain this, further analysis is necessary, as follows.

During tribocorrosion, the synergism between wear and corrosion arises from wear-induced corrosion (ΔC) and corrosion-induced wear (ΔW) [23,26]. Thus, the term, S , is the sum of ΔC and ΔW :

$$S = \Delta C + \Delta W \quad (3)$$

where, by using Equation (2), ΔC can be calculated from the measured corrosion current during sliding (subtracted by the corrosion current measured under no-sliding conditions). Using the current density data in Table 3, ΔC is calculated for both specimens and then ΔW is obtained from Equation (3). The results are listed in the last two columns of Table 4. It can be seen that ΔC and ΔW have positive values, suggesting that, at OCP, corrosion is accelerated by wear and wear is accelerated by corrosion in both specimens. For the normalized specimen, the contribution of wear-accelerated corrosion (ΔC) to the synergism is more significant than the contribution of corrosion accelerated-wear (ΔW). On the other hand, for the γ' -Fe₄N layer, corrosion accelerated-wear (ΔW) contributes more to the synergism. The ΔW value from the γ' -Fe₄N layer is even larger than that from the normalized specimen. This suggests that the corrosion-wear products trapped at the contact interface can serve as third-body particles to cause accelerated wear of the γ' -Fe₄N layer, as evidenced by the many wide scratch marks and the existence of corrosion-wear products on the sliding surface shown in Figure 8c,d.

Although it is not possible to quantitatively estimate the relative contribution of various TMR components at the anodic potential by using Equations (1) to (3), judging from the measured currents (Figure 9) and sliding track morphology (Figures 10 and 11), it can be deduced that corrosion and wear–corrosion synergism play increasing roles in TMR from both specimens. For the PN specimen, the local breakdown of the γ' -Fe₄N layer can lead to much accelerated corrosion in the form of pitting corrosion, which in turn can lead to accelerated mechanical wear [38]. Thus, like other surface coatings for corrosion and wear protection, there is always an issue concerning the sustainability of the coating system under harsh loading and environmental conditions [39].

5. Conclusions

1. In the NaCl-containing solution, both the normalized mild steel and γ' -Fe₄N layer are in the active state in the anodic region. The γ' -Fe₄N layer has the ability to reduce metal dissolution and improve corrosion resistance of mild steel.
2. At the cathodic potential, where mechanical wear dominates, the γ' -Fe₄N layer can reduce total material removal by 37% due to its higher hardness than that of normalized mild steel.
3. At open circuit potential, where both mechanical wear and corrosion are involved, the γ' -Fe₄N layer has the ability to reduce mechanical wear, corrosion and the synergy between wear and corrosion due to its higher hardness and better resistance to metal dissolution, such that the total material removal is reduced by 34% as compared to that from the normalized mild steel.
4. At the anodic potential, where corrosion plays an increasing role, the γ' -Fe₄N layer can reduce total material removal by 87%. However, local breakdown of the γ' -Fe₄N layer can happen in the sliding track, leading to accelerated pitting corrosion.
5. The γ' -Fe₄N layer has the ability to improve the tribocorrosion behavior of mild steel in the NaCl-containing solution under all test conditions, provided that the layer is not worn through or broken down locally during the tribocorrosion process. However, there is a concern regarding the sustainability of the layer when localized breakdown or wearing-through occurs, which can lead to accelerated pitting and accelerated material removal.

Author Contributions: Methodology, Y.S.; Experimentation, Y.S. and R.B.; Investigation, Y.S. and R.B.; writing—original draft preparation, Y.S.; writing—review and editing, R.B. All authors have read and agreed to the published version of the manuscript.

Funding: This research received no external funding.

Data Availability Statement: The original data of this work is available from the authors upon reasonable request.

Conflicts of Interest: The authors declare no conflict of interest.

References

1. Staines, A.M.; Bell, T. Technological importance of plasma-induced nitrided and carburized layers on steel. *Thin Solid Films* **1981**, *86*, 201–212. [[CrossRef](#)]
2. Spies, H.J.; Thien, H.L.; Biermann, H.B. Controlled nitriding. *Met. Sci. Heat Treat.* **2004**, *46*, 272–276. [[CrossRef](#)]
3. Lightfoot, B.J.; Jack, D.H. Kinetics of nitriding with and without white-layer formation. In *Heat Treatment '73*; The Metals Society: Metals Park, OH, USA, 1973; Republished in the Source Book on Nitriding; American Society for Metals: Metals Park, OH, USA, 1977; pp. 248–254.
4. Mittemeijer, E.J.; Somers, A.L. (Eds.) *Thermochemical Surface Engineering of Steels*; Elsevier Woodhead Publishing: Sawston, Cambridge, 2015.
5. Menthe, E.; Rie, K.T.; Schultze, J.W.; Simson, S. Structure and properties of plasma-nitrided stainless steel. *Surf. Coat. Technol.* **1995**, *74–75*, 412–416. [[CrossRef](#)]
6. Zhang, L.; Shao, M.; Zhang, Z.; Yi, X.; Yan, J.; Zhou, Z.; Fang, D.; He, Y.; Li, Y. Corrosion behaviour of nitrided layer of Ti₆Al₄V titanium alloy by hollow cathodic plasma source nitriding. *Materials* **2023**, *16*, 2961. [[CrossRef](#)] [[PubMed](#)]
7. Zhecheva, A.; Malinov, S. Titanium alloys after surface gas nitriding. *Surf. Coat. Technol.* **2006**, *201*, 2467–2474. [[CrossRef](#)]
8. Buchwalder, A.; Bocker, J.; Hegelmann, E.; Klemm, V. Investigations on the microstructure of an aluminium nitride layer and its interface with the aluminium substrate (Part I). *Coatings* **2022**, *12*, 618. [[CrossRef](#)]
9. Visuttipitukul, P.; Aizawa, T.; Kuwahara, H. Advanced plasma nitriding for aluminium and aluminium alloys. *Mater. Trans.* **2003**, *44*, 2695–2700. [[CrossRef](#)]
10. Sun, Y. Kinetics of layer growth during plasma nitriding of nickel based alloy Inconel 600. *J. Alloys Compd.* **2003**, *351*, 241–247. [[CrossRef](#)]
11. Tao, X.; Kavanagh, J.; Li, X.; Dong, H.; Matthews, A.; Leyland, A. An investigation of precipitation strengthened Inconel 718 superalloy after triode plasma nitriding. *Surf. Coat. Technol.* **2022**, *442*, 128401. [[CrossRef](#)]
12. Luo, X.; Li, X.; Sun, Y.; Dong, H. Tribocorrosion behaviour of S-phase surface engineered medical grade Co-Cr alloy. *Wear* **2013**, *302*, 1615–1623. [[CrossRef](#)]
13. Purandare, Y.; Shukla, K.; Sugumaran, A.; Ehiasarian, A.; Khan, I.; Hovsepian, P. Improving tribocorrosion resistance of a medical grade CoCrMo alloy by the novel HIPIMS nitriding technique. *J. Sci. Adv. Mater. Devices* **2023**, *8*, 100570. [[CrossRef](#)]
14. Spies, H.J. Corrosion behaviour of nitrided, nitrocarburised and carburised steels. In *Thermochemical Surface Engineering of Steels*; Mittemeijer, E.J., Somers, A.L., Eds.; Elsevier Woodhead Publishing: Sawston, Cambridge, 2015.
15. Mittemeijer, E.J. Nitriding of binary and ternary iron-based alloy. In *Thermochemical Surface Engineering of Steels*; Mittemeijer, E.J., Somers, A.L., Eds.; Elsevier Woodhead Publishing: Sawston, Cambridge, 2015.
16. Jasinski, J.J.; Kurpaska, L.; Frazek, T.; Lubas, M.; Sitarz, M. Structural characterisation of fine γ' -Fe₄N nitrides form by active screen plasma nitriding. *Metals* **2020**, *10*, 1656. [[CrossRef](#)]
17. Bell, T.; Loh, N.L. The fatigue characteristics of plasma nitrided three Pct Cr-Mo steel. *J. Heat Treat.* **1982**, *2*, 232–237. [[CrossRef](#)]
18. Kato, H.; Eyre, T.S.; Ralph, B. Wear mechanism map of nitrided steel. *Acta Metall. Mater.* **1994**, *42*, 1703–1713. [[CrossRef](#)]
19. Bell, T.; Sun, Y. Load bearing capacity of plasma nitrided low alloy steel under combined rolling-sliding contact. *Surf. Eng.* **1990**, *6*, 133–139. [[CrossRef](#)]
20. Boztepe, E.; Alves, A.C.; Ariza, E.; Rocha, L.A.; Cansever, N.; Toptan, F. A comparative investigation of the corrosion and tribocorrosion behaviour of nitrocarburized, gas nitrided, fluidized-bed nitrided, and plasma nitrided plastic mould steel. *Surf. Coat. Technol.* **2018**, *334*, 116–123. [[CrossRef](#)]
21. Ram Mohan Rao, K.; Nouveau, C.; Lakshman, S.; Muralidhar, P.; Trinadh, K. Effect of low and high temperature plasma nitriding on electrochemical corrosion of steel. *Mater. Today Proc.* **2020**, *39*, 1367–1371. [[CrossRef](#)]
22. Valdes, J.; Huape, E.; Oseguern, J.; Ruiz, A.; Ibarra, J.; Bernal, J.L.; Medina, A. Effects of plasma nitriding in corrosion behaviour of an AISI 4140 steel using a seawater medium solution. *Mater. Lett.* **2022**, *316*, 131991. [[CrossRef](#)]
23. Watson, S.W.; Friedersdorf, F.J.; Madsen, B.W.; Gramer, S.D. Methods of measuring wear-corrosion synergism. *Wear* **1995**, *181–183*, 476–484. [[CrossRef](#)]
24. Ponthiaux, P.; Wenger, F.; Drees, D.; Celis, J.P. Electrochemical techniques for studying tribocorrosion processes. *Wear* **2004**, *256*, 459–468. [[CrossRef](#)]
25. Munoz, A.I.; Espallargas, N.; Mischler, S. (Eds.) *Tribocorrosion*; Springer: Cham, Switzerland, 2020.

26. Mischler, S. Triboelectrochemical techniques and interpretation methods in triborrosion: A comparative evaluation. *Tribol. Int.* **2008**, *41*, 573–583. [[CrossRef](#)]
27. Landolt, D.; Mischler, S.; Stemp, M. Electrochim. Electrochemical methods in tribocorrosion: A critical appraisal. *Electrochim. Acta* **2001**, *46*, 3913–3929. [[CrossRef](#)]
28. Mindivan, F.; Aktas, G.R.; Bayram, A. Influence of plasma nitriding on dry wear, corrosion and tribocorrosion performance of 17-4 precipitation hardening stainless steel. *Mater. Werkst.* **2022**, *53*, 963–978. [[CrossRef](#)]
29. Li, X.; Dou, W.; Tian, L.; Dong, H. Combating the tribo-corrosion of LDX2404 lean duplex stainless steel by low temperature plasma nitriding. *Lubricants* **2018**, *6*, 93. [[CrossRef](#)]
30. Hacısalihoglu, I.; Yildiz, F.; Celik, A. Tribocorrosion behavior of plasma nitrided Hardox steels in NaCl solution. *Tribol. Int.* **2018**, *120*, 434–445. [[CrossRef](#)]
31. Wong-Angel, W.D.; Martinez-Trinidad, J.; Campos-Silva, V.; Hernandez-Hernandez; Silva-Rivera, U.S.; Garcia-Leon, R.A. Wear-corrosion synergy on Din-16MnCr₅ steel under nitriding and post-oxidizing treatments. *J. Bio-Tribo-Corros.* **2021**, *7*, 83. [[CrossRef](#)]
32. Takahashi, T.; Burghaus, J.; Music, D.; Dronskowski, R.; Schneider, J.M. Elastic properties of γ' -Fe₄N probed by nanoindentation and ab initio calculation. *Acta Mater.* **2012**, *60*, 2054–2060. [[CrossRef](#)]
33. Sun, Y.; Bailey, R. Comparison of wear performance of low temperature nitrided and carburized 316L stainless steel under dry sliding and corrosive-wear condition. *J. Mater. Eng. Perform.* **2022**, *32*, 1238–1247. [[CrossRef](#)]
34. Casar, J.; Malia, B.; Mazzonello, A.; Karl, A.; Buhagiar, J. Improved tribocorrosion resistance of a CoCrMo implant material by carburising. *Lubricants* **2018**, *6*, 76. [[CrossRef](#)]
35. Rasool, G.; Shafei, Y.E.; Stack, M.M. Mapping tribo-corrosion behaviour of Ti-6Al-4V Eli in laboratory simulated hip joint environments. *Lubricants* **2020**, *8*, 69. [[CrossRef](#)]
36. Antunes, R.A.; Ichikawa, R.U.; Martinez, L.G.; Costa, I. Characterisation of corrosion products on carbon steel exposed to natural weathering and to accelerated corrosion tests. *Int. J. Corros.* **2014**, *2014*, 419570. [[CrossRef](#)]
37. Fonna, S.; Ibrahim, I.B.M.; Gunawarman; Huzni, S.; Lksan, M.; Thalib, S. Investigation of corrosion products formed on the surface of carbon steel exposed in Banda Aceh's atmosphere. *Heliyon* **2021**, *7*, e06608. [[CrossRef](#)]
38. Jiang, J.; Stack, M.M.; Neville, A. Modelling the tribo-corrosion interaction in aqueous sliding conditions. *Tribol. Int.* **2002**, *35*, 669–679. [[CrossRef](#)]
39. Sun, Y.; Dearnley, P.A.; Bertram, M. Response of duplex Cr(N)/S and Cr(C)/S coatings on 316L stainless steel to tribocorrosion in 0.89% NaCl solution under plastic contact conditions. *J. Biomed. Mater. Res. Part B* **2017**, *105*, 1503–1513. [[CrossRef](#)] [[PubMed](#)]

Disclaimer/Publisher's Note: The statements, opinions and data contained in all publications are solely those of the individual author(s) and contributor(s) and not of MDPI and/or the editor(s). MDPI and/or the editor(s) disclaim responsibility for any injury to people or property resulting from any ideas, methods, instructions or products referred to in the content.